

**Phase engineering of Transition Metal Dichalcogenides**

Journal:	<i>Chemical Society Reviews</i>
Manuscript ID:	CS-REV-02-2015-000151.R1
Article Type:	Review Article
Date Submitted by the Author:	03-Apr-2015
Complete List of Authors:	Voiry, Damien; Rutgers University, Materials Science and Engineering Mohite, Aditya; Los Alamos National Laboratory, Chhowalla, Manish; Rutgers University, Ceramics and Materials Engineering

Phase engineering of Transition Metal Dichalcogenides

Tutorial review

Damien Voiry¹, Aditya Mohite², Manish Chhowalla¹

1. Materials Science and Engineering, Rutgers University, 607 Taylor Road, Piscataway, NJ 08854 USA
2. Materials Physics and Application Division, Los Alamos National Laboratory, Los Alamos, NM 87545, USA.

Abstract

Transition metal dichalcogenides (TMDs) represent a family of materials with versatile electronic, optical, and chemical properties. Most TMD bulk crystals are van der Waals solids with strong bonding within the plane but weak interlayer bonding. The individual layers can be readily isolated. Single layer TMDs possess intriguing properties that are ideal for both fundamental and technologically relevant research. We review the structure and phases of single and few layered TMDs. We also describe recent progress in phase engineering in TMDs. The ability to tune the chemistry by choosing unique combination of transition metal and chalcogen atoms along with controlling their properties by phase engineering allows new functionalities to be realized with TMDs.

I. Structure of Transition Metal Dichalcogenides

A. 1T, 2H, 3R polymorphs

Many transition metal dichalcogenides (TMDs) have layered structure similar to graphite. In TMDs, one unit layer is 3-atoms thick in which the transition metal (M) atom is sandwiched between two chalcogens (X), giving the stoichiometry MX_2 ¹. The intralayer bonds are covalent, whereas the interlayer bonds between two MX_2 slabs are typically Van der Waals. The weak Van der Waals bonds allow exfoliation of TMDs down to single layers². Given the relatively large number of transition metal and chalcogen combinations that can be realized, TMDs with a variety of electronic structures can be realized^{1,3,4}. In contrast to graphene or silicon where the electronic properties are based on hybridization of s and p orbitals, the

electronic structure of TMDs depends on the filling of d orbitals of the transition metals. Transition metals in MX_2 compounds have an oxidation state of +4 and the chalcogens have an oxidation state of -2. Thus the number of d orbital electrons varies between 0 and 6 for group 4 to group 10 TMDs, respectively. In addition to diverse electronic properties that can be achieved by choosing the appropriate combinations of the M and X elements, different phases in single layer TMDs can also be realized. A single layer of TMDs can have a trigonal prismatic phase or an octahedral phase. The trigonal prismatic phase, is also referred to as the 2H phase (or 1H in the case of a single-layer) and can be described by a hexagonal symmetry (D_{3h} group) and corresponds to a trigonal prismatic coordination for the metal atoms. This geometry means that in single-layers, the sulfur atoms are vertically aligned along the z-axis and the stacking sequence is then AbA where A and b denote chalcogen and metal atoms, respectively (Figure 1a). The octahedral phase has a tetragonal symmetry (D_{3d}) and corresponds to an octahedral coordination of the metal atoms. In the octahedral phase, conventionally referred to as the 1T phase, one of the sulfur layer is shifted compared to the others resulting in an AbC stacking sequence (Figure 1b). The filling of the d orbitals of the metal directly influences the atomic structure of the TMD layers. For the 1H phase, the d orbital splits into 3 degenerate states d_{z^2} , $d_{x^2-y^2,xy}$ and $d_{xy,yz}$ with an energy gap of ~ 1 eV between the d_{z^2} and $d_{x^2-y^2,xy}$ orbitals. For the tetragonal symmetry of the 1T phase, the d orbitals of the metal degenerate into $d_{xy,yz,zx}$ (t_{2g}) and $d_{x^2-y^2,z^2}$ (e_g) orbitals. Up to 6 electrons can fill the e_{2g} orbital. Since the p orbitals of chalcogens are located at much lower energy than the Fermi level, only the filling of the d orbitals determines the nature of phases in MX_2 compounds. Completely filled orbitals give rise to semiconducting behavior while partial filling induces metallic behavior. The type of symmetry of the single layer also strongly depends on the filling of d orbitals. The Group 4 (d^0) TMDs and most of the group 6 (d^2) TMDs have trigonal prismatic phases. Group 5 (d^1) TMDs can have both trigonal prismatic or

octahedral phases whereas group 7 TMDs have typically distorted octahedral structure (Figure 1c). Group 10 TMDs (d^6) have an octahedral phase.

Typically in single layer TMDs, one of the two possible polytypes are thermodynamically stable. Phase engineering can be used to change the polytype as well as the electronic properties of the materials. In addition to the 1T and 1H phases, 2 different ways of stacking the 1H layers can be achieved, imparting hexagonal symmetry (2H phase, symmetry D_{4h}^6) with a stacking sequence of AbA BaB or rhombohedral symmetry (3R, symmetry C_{3v}^5) with the stacking sequence of AbA CaC BcB (Figure 1d). Stacking in 1T layer produces AbC AbC (Figure 1e) sequence. These heterogeneities in stacking order can introduce defects but also lead to interesting new phenomena due to breaking of symmetry.

B. TMD Heterostructures

The phase of single-layer TMDs depends strongly on the d orbital electronic density of the transition metal. Tuning the filling of the d orbital enables phase engineering in TMDs. Several examples of phase modification using chemistry have been reported for group 6 TMDs such as MoS_2 , $MoSe_2$ and WS_2 ⁵⁻⁹. Early experiments from Py et al. demonstrated the formation of the metallic 1T phase of MoS_2 upon lithium intercalation¹⁰, which induces reduction of MoS_2 and increases the electron density in the d orbital. As a consequence, group 6 TMDs with the 1T phase are typically negatively charged¹¹. Similarly the lithiation of TaS_2 induces a phase change from semiconducting 1T phase to metallic 2H¹². Generally, phase transformation in exfoliated single-layer TMDs is not complete and leads to layers containing fraction of both 2H and 1T phases¹³. Furthermore it has been observed in the case of group 6 TMDs that the 1T phase does not correspond to the ideal (a x a) 1T phase of TiS_2 but rather to a distorted 1T phase^{8,14-16}. The 1T phase for group 6 TMDs is unstable. However, the stability can be improved by the formation of a superlattice structure and/or by stabilizing the excess

charge on the surface of the reduced TMDs. Four different superstructures have been proposed: a tetramerization ($2a \times 2a$), a trimerization ($\sqrt{3}a \times \sqrt{3}a$), and a zigzag chain ($2a \times a$). The identification of the type of distortion has been debated for a long time. Heising et al. have elucidated the distortion of restacked 1T MoS₂ and 1T WS₂ using electron diffraction. Their observations have elucidated that the distorted structure of restacked 1T MoS₂ (WS₂) forms zig-zag chains similar to the structure of WTe₂ with short M-M distance of 0.27 nm and 0.29 nm for W and Mo, respectively¹⁷. These distances are substantially shorter than typical values of the 2H phase: 0.315 and 0.312 nm for WS₂ and MoS₂, respectively. These results are in good agreement with STM measurements by Qin et al¹⁵. More recently, HAADF-STEM experiments have enabled direct observation of the atomic structure (Figure 1f) of the different phases^{13,18,19}. STEM studies of single-layer exfoliated MoS₂/WS₂ after lithium intercalation illustrate the zig-zag chains ($2a \times a$) from the distorted WTe₂-like 1T phase of MoS₂ and WS₂ together with ideal 1T TiS₂-like phase. Other EXAFS and X-ray diffraction experiments on reduced MoS₂ dispersed in solution or intercalated with hydroxide molecules or metal atoms have suggested the existence of ($2a \times a$) superstructure in the solution. The ($\sqrt{3}a \times \sqrt{3}a$) superstructure has been reported from oxidized K_x(H₂O)_yMoS₂ (without the formation of Mo⁶⁺) or restacked 1T MoS₂ treated with Br₂^{14,17}. Similar treatments performed on WS₂ do not induce any observable changes in the superstructure of 1T WS₂, while the zig-zag distortion is observed in all the cases¹¹.

Interestingly, some TMDs are naturally disordered. 1T WTe₂ (group 6) and 1T ReS₂ (group 5) are good examples of such distorted TMDs with each layer consisting of zig-zag chains of transition metal atoms. Tongay et al. have shown that each layer in a bulk crystal of ReS₂ behaves as monolayer due to the distortion in the 1T phase²⁰. It has been recently shown that reduction of ReS₂ further increases the distortion and generates Re₄ rhombus clusters (Figure 1g)²¹.

C. Strain in Distorted TMDs

The distorted structure of 1T TMDs induces modification of the Metal-Metal bond distance and thus affects the electronic structure. For example, ReS₂ with 3 electrons in the d orbital is expected to be metallic. However, the strong distortion of the layers forming infinite zig-zag chains of Re atoms opens an energy gap in the band structure as shown by Keretz and Hoffmann²². ReS₂ behaves as direct band gap semiconductor with a band gap of 1.35 eV and 1.45 eV for bulk and monolayer, respectively²⁰. In addition to the distortion, monolayers of TMDs can be strained. STEM observations of distorted 1T WS₂ have shown an overall isotropic strain of ~ 3%, in agreement with previous X-ray diffraction measurements²³. DFT simulations of the density of states for distorted 1T phase WS₂ have revealed that strain enhances the density of states near the Fermi level²⁴. Recently several groups have predicted that zig-zag chains in 1T phase MoS₂ should open up a small gap of 22-45 meV^{25,26}.

Strain engineering is an intense field of research for the TMD community. DFT calculations have predicted that shear or tensile strain²⁶ is another way to tune the properties²⁷⁻³². Interestingly, biaxial tensile strain leads to a red-shift in the band gap of semiconducting TMDs. Direct to indirect band gap transition are also predicted with stretching of TMDs, making strain engineering particularly interesting for controlling optoelectronic properties. For isotropic tensile strain of > 11%, 1H MoS₂ and WS₂ become metallic whereas with uniaxial strain, MoS₂ and WS₂ retain their semiconducting properties^{27,28}. Strain has also been shown to improve the catalytic activity of TMDs^{18,33}. Calculations related to strain have also been performed on hetero-bilayers of MoS₂/MX₂³⁴. Experimentally, strain on single-, bi- and tri-layers of MoS₂ has been applied by folding the crystal or bending the substrate³⁵⁻³⁹. A decrease in the band gap by ~ 45 meV per percent of applied strain has been measured. In addition, direct to indirect transition in the band gap has been observed above ≈ 1% strain (Figure 2a)³⁵.

D. Stacking of TMD Layers

Stacking sequence of 1H TMDs can generate the 2H (AB sequence) or 3R (ABC sequence) structures. The ability to grow or exfoliate a variety of single layer TMDs opens up possibilities of restacking them in desired sequences to achieve novel heterostructures^{34,40–45} (Figure 2b). Restacked or folded single layer MoS₂ possesses different properties compared to monolayered and bi-layer 2H MoS₂. Stacking sequence can break the inversion symmetry of bilayer TMDs, allowing an additional pathway for tuning the optical, electronic and spintronic properties of TMDs⁴⁶. The energy of the indirect transition varies from 1.49 eV to 1.62 eV for twist angles of 0 and 30° (Figure 2c)⁴⁷. This is attributed to interlayer coupling, which depends on the twist angle between the top and bottom layer of MoS₂. Restacked bilayer MoS₂ shows strong dependence on interlayer spacing. In the band structure, Mo-d states are found at the K points whereas a mixture of Mo-d_{z²} and S-p_z are found in the valence band at the Γ point. S-p_z states are dependent on the interlayer stacking, and as a consequence, the energy state at Γ point is more sensitive to the interlayer coupling than the K point. Additionally the concentration of trions and excitons are also found to depend on the twist angle⁴⁸. Similar results have been observed from folded MoS₂ although the control of over the twist angle is more difficult.

E. Grain Boundaries in TMDs

Grain boundaries have been observed in single layer TMD crystals using dark-field TEM, STEM or second harmonic generation^{49–52}. Grain boundary of MoS₂ displays unique properties, which differ significantly from the properties of ideal monolayer. STEM observations of TMDs allow direct observation of grain boundaries in monolayered crystals^{49,50,53}. Due to the unique structure of TMDs, various types of dislocations have been observed; such as 5|7 fold rings similar to those reported for graphene. In addition 4|4, 4|6 and

6|8 fold rings⁵³ have also been observed. Grain boundaries at different angles: 4|4 and 4|8 fold rings at 60° versus 6|8 and 5|7 fold rings at 18.5° have been found to possess different electronic properties (Figure 1h). Predictions of local density of states (LDOS) suggest that the 60° grain boundaries with 4|4 and 4|8 structures are metallic, which can potentially be used to fabricate novel heterostructures for electronics. Other properties such as magnetism are possible from MoS₂ grain boundaries⁵⁴. Yakobson and co-workers have reported that 5|7 dislocations are expected to be ferromagnetic and the intensity of the magnetism depends on the tilt angle of the dislocations whereas 4|8 dislocations at tilt angles higher than 48° are favored and are antiferromagnetic⁵⁴.

F. Hybrids with Different Chalcogens, and Different Transition Metals

The synthesis of single layer crystals by chemical vapor deposition has opened new directions towards realizing alloys of TMDs either by varying the transition metal or chalcogen atoms during growth. For example, selenide doped MoS₂: MoS_{2(1-x)}Se_{2x} has been obtained via a direct synthesis⁵⁵⁻⁵⁷. Typically the doping of MoS₂ with selenide enables modification of the band gap of MoS_{2(1-x)}Se_{2x} from 1.85 eV ($x = 0$) to 1.55 eV ($x = 1$) (Figure 2d). The PL emission energy varies linearly between the two values with the S concentration, in perfect agreement with theoretical predictions⁵⁶. STEM observations of MoS_{2(1-x)}Se_{2x} have revealed that the selenium atoms are randomly introduced in the MoS₂ crystal structure⁵⁶.

Alternatively, MoS_{2(1-x)}Se_{2x} can also be obtained by the selenization of already grown 1H MoS₂ crystals. The Se-doping efficiency increases with increasing temperature from 600°C up to 900°C, which allows for tuning of the band gap from 1.86 eV to 1.57 eV⁵⁸. Alloying two or more transition metals has also been shown to tune the TMD properties^{59,60}. Individual dopants have been observed by electron microscopy modifying the local density of states and potentially the catalytic activity of the materials^{61,62}. Controlled alloying has been more challenging but recent publications have demonstrated the successful synthesis of single layer

$\text{Mo}_{(1-x)}\text{W}_x\text{S}_2$ obtained by mechanical exfoliation of bulk crystal grown by chemical vapor transport^{63–66}. The presence of both Mo and W atoms in the layers has been confirmed by electron energy loss microscopy. STEM observations have revealed random distribution of Mo and W atoms in the crystal⁶³. $\text{Mo}_{(1-x)}\text{W}_x\text{S}_2$ have a hexagonal symmetry although some distorted atomic structure has been observed using STEM⁶⁶. The PL emission of $\text{Mo}_{(1-x)}\text{W}_x\text{S}_2$ was found to vary from 1.82 eV (for $x = 0.2$) to 1.99 eV (for $x = 1$) and the presence of the B exciton peak in the PL spectra suggests that the spin-orbit coupling remains similar to that observed for pristine MoS_2 .

Due to the high melting temperature of transition metal source (typically metal oxide), the synthesis of TMDs from mixed metals is difficult. The relatively large difference between the melting temperature of precursors can however be used to grow TMD crystals with alternating transition metals. Duan et al. have successfully grown MoSe_2 - WSe_2 crystals with lateral heterojunction using MoSe_2 and WSe_2 powder as precursors (Figure 2e)⁴⁵. During epitaxial growth, MoSe_2 triangles are first deposited on the substrate. The WSe_2 growth is catalyzed from MoSe_2 edges due to small lattice mismatch between the materials.

Interestingly there is progressive transition from MoSe_2 to WSe_2 (Figure 2f) and the PL signals from the interface between the two domains consist of a mixture of PL signals from each material. The wide combination of chalcogen and transition metal elements allow for infinite number of combinations for the synthesis of TMD alloys.

G. Defects and Doping in TMDs

Beyond grain boundaries, other types of defects can be observed in TMD crystals. Because of their physical dimensions, 2D materials are very sensitive to the presence of defects in the crystalline structure. The influence of defects has been intensely studied using both DFT calculations and experimental approaches^{53,67–71}. Atomic vacancies are major sources of defects in TMDs. Contrary to graphene, which is made of only one layer of carbon, the

alternating X-M-X increase the variety of defects in TMDs. Chalcogen vacancies, metal vacancies or both have been observed experimentally by STEM⁵³. Chalcogen and metal vacancies are thought to induce profound modification of the electronic structure. For example, in the case of MoS₂, S vacancies are thought to introduce n-type doping whereas Mo vacancies are expected to induce p-type doping. The n-type behavior of MoS₂ is commonly attributed to the lower concentration of S in MoS₂ crystals. Recently McDonnell et al. have observed local p- and n-type regions in mechanically exfoliated MoS₂, suggesting that the local stoichiometry might vary significantly from the average macroscopic stoichiometry⁶⁷. Tongay et al. have reported an additional peak at ~ 1.78 eV in MoS₂ arising from defects in group 6 TMDs⁶⁸. The new peak is attributed to bound excitons formed by localized excitons at defect sites. S vacancies can coordinate thiol molecules, which could open new directions for self healing^{69,70}.

Edges of MoS₂ and WS₂ are known to be highly active for hydrogen evolution. TMDs can have metal or chalcogen terminated edges. Van der Zande and coworkers have observed that Mo edges of CVD-grown MoS₂ are usually more sharp and straight than S edges⁵⁰. Edges of MoS₂ and WS₂ can contain 0 %, 50 % or 100 % sulfur, depending on the synthesis conditions. For example, in the case of industrial catalysts grown on graphitic carbon, MoS₂ nanoclusters have been found to have 50% coverage of Mo edges, whereas large clusters with more than 6 Mo atoms at edges are generally fully sulfur passivated⁷¹. Recent STEM observations of molybdenum edges of CVD 1H MoS₂ revealed that edges consist of both bare and 50% S covered edges⁵³.

II. Synthesis and Characterization of TMDs

The different synthesis strategies for single layer TMDs can be divided into 3 categories: mechanical exfoliation, liquid exfoliation, epitaxial growth or chemical vapor deposition. Each of these strategies offers varying quality and yield.

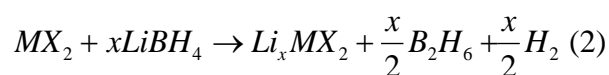
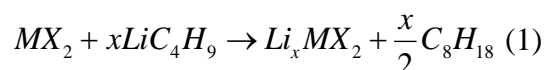
H. Phase Engineering via Alkali Metal Intercalation

Most experiments on phase engineering of TMDs have used lithium intercalated TMDs. During lithium intercalation, there is an electron transfer from the reducing agent to the structure of TMDs and thus the electronic density of the d orbital of the transition metal increases. This induces a destabilization of the pristine 2H phase and favors the phase transition to the metallic 1T phase. The first synthesis of single TMDs was reported in the 1980's using chemical exfoliation via lithium intercalation¹⁰. Original work in Li intercalation in TMDs was motivated by new battery electrode materials⁷². Pioneering work was performed by Py and Haering in 1983¹⁰ and lithium intercalated MoS₂ is among the most widely studied TMD^{73,74} material. Recent theoretical reports on the intercalation of MoS₂ have shown that the 1T phase becomes more stable than the 2H phase with an excess charge on the exfoliated nanosheets of 0.2-0.4^{75,76}. Moreover DFT calculations have elucidated that 1T phase consists of a distorted structure rather than the ideal TiS₂-like octahedral phase. Kan et al. have predicted that clustering of the metal atoms starts as soon as the octahedral phase is favored⁷⁶. At 100% intercalation, the crystal structure of MoS₂ corresponds to a distorted octahedral phase with rhombohedral Mo–Mo chains. In-situ HR-TEM and FFT pattern obtained from Li-intercalated MoS₂ have confirmed the clustering of Mo atoms into a (2a x 2a) superstructure, which can be described as a combination composed of a variety of sublattices, including (a x a), (2a x a), ($\sqrt{3}a \times \sqrt{3}a$), ($\sqrt{3}a \times a$) and (2a x 2a)⁷⁷. After exfoliation, the distortion evolves into (2a x a) zig-zag WTe₂-type structure as observed by STEM, although the presence of undistorted TiS₂-like structure has also been identified^{13,17}.

TMDs can be intercalated chemically using lithium reactants, typically n-butyllithium diluted in hexane^{6,78,79}. After 48 hours of reaction at room temperature or at reflux, the Li intercalated materials are filtered and washed with hexane in order to remove the excess of butyllithium and other organic byproducts of the reaction (see reaction (1) below). The electron transfer

from butyl to the TMD layers implies the insertion of Li^+ in the Van der Waals gap.

Alternatively the lithium intercalation can be achieved in solid state by mixing TMD powder with lithium borohydrate (reaction (2) below)^{21,80,81}. Powders are mixed together and reaction is performed at 350°C for 12 hours. The absence of solvents and the fact that the byproduct of the reaction, B_2H_6 and H_2 , are gaseous, leaves intercalated TMDs clean and free of chemicals used for the phase conversion.



TMDs can also be intercalated electrochemically. Zhang's group has demonstrated the synthesis of intercalated TMDs prepared via lithium electrochemical intercalation⁸². They improved this process further by using the bulk TMDs as cathode materials and Li metal as the anode⁸³. Once intercalated, Li_xMX_2 are spontaneously soluble in water. The immersion of Li_xMoS_2 powder in water generates H_2 and potentially H_2S . The mechanism for the exfoliation is not completely elucidated. However, it most likely based on the combination of H_2 bubbling, which separates the nanosheets, and the presence of negative charges on the nanosheets, which stabilizes the exfoliated nanosheets in colloidal solutions¹¹. It is worth noting that the yield of single layer nanosheets prepared via lithium intercalation is high, about 10-20% of the starting bulk powder with large majority of the nanosheets in solution as single layers. Although water is the best solvent to achieve complete exfoliation of intercalated TMDs, few attempts have been carried out in organic solvents such as formamide and N-methylformamide⁸⁴. The absence of Moiré pattern in the STEM images confirms the single-layer nature of the exfoliated materials. Eda and co-workers have studied the heterostructure of exfoliated 1T MoS_2 prepared via Li-intercalation¹³. Three phases have been

observed: the 1H phase, the non-distorted (TiS₂-like) 1T phase and the distorted (2a x a) 1T phase consisting of zig-zag chain (WTe₂-like structure). The presence of the zig-zag Mo-Mo chains is in good agreement with DFT calculations. The presence of different phases is confirmed by the FFT of the STEM images. Higher amount of distorted 1T phase have been found in the case of single WS₂ prepared the same way²⁴. STEM reveals that existence of coherent interface between metallic (1T phase) and semiconducting (2H phase) domains.

Other than electron microscopy, identification of the different phases of SL or few-layer TMDs is non-trivial. However, several techniques such as photoluminescence, Raman spectroscopy and X-ray photoelectron electron spectroscopy (XPS) offer fast and relatively precise ways to characterize the heterostructures in TMDs. Changing the phase of TMDs induces changes in the optoelectronic properties. Emergence or extinction of photoluminescence can easily be detected⁷⁹. Raman spectroscopy is a powerful tool for estimating the thickness and the phases of the TMD crystals⁸⁵. Raman spectra of 1T MoS₂ displays additional modes: J₁, J₂ and J₃ in addition to the E_{2g}¹ (in-plane) and A_{1g} (out of plane modes) of 2H MoS₂ (Figure 3a)^{7,8}. At higher content of 1T phase, the intensity of the E_{2g}¹ peak decreases. J₁, J₂ and J₃ are attributed to the superlattice structure of the distorted 1T phase⁷. Recent work from Calandra has validated the vibrational modes of each of the peaks in 1T MoS₂²⁵. The J₁ mode is the in-plane shearing mode of one side of the zig-zag chain relative to the other. The J₂ mode corresponds to the shifts of the S-atom layers with respect to the Mo atoms whereas the J₃ mode involves the stretching of one side of the zig-zag chain relative to the other with a slight out-of-plane component. In addition to Raman, XPS can also identify the 1T and 1H (2H) phases of given TMDs. XPS is sensitive to the differences of the Fermi level between the 1T and the 1H (2H) phases as reported by Papageorgopoulos and Jaegerman⁸⁶. In chemically exfoliated group-6 TMDs, the 1T signal is down-shifted by ~ 0.8 eV relative to the 1H phase. The deconvolution of the high-resolution spectra from the metal

and the chalcogen enables the quantitative estimation of the 1T and 2H phase (Figure 3b)^{24,79}. However the type of 1T phase: ideal undistorted or distorted can not be elucidated by XPS and so far only STEM can unambiguously identify the atomic structure of the 1T phase.

Alternate routes based on intercalation have also been reported using other alkali metals^{84,87}. Systematic studies of exfoliation of TMDs with the different counter-ions has been carried by Zheng and co-workers using naphthalene as reducing agent instead of butyl in the case of butyllithium⁸⁷. The crystals of TMDs were first pre-exfoliated using hydrazine before intercalation with different alkali metals. This route produces large single nanosheets with lateral dimension $> 5 \mu\text{m}$. The highest quality of exfoliated was obtained using Na intercalated TMDs. Although the phase transition has not been investigated, similar phase transition upon filling the d orbitals of the transition metals is expected during the reaction with naphthalene.

I. Alternative Strategies for Phase Engineering

The emergence of phase engineered TMDs has driven efforts to develop alternative synthetic routes. Lin and coworkers reported the synthesis of undistorted 1T MoS₂ by using electron-beam⁶². With e-beam irradiation, the 2H phase converts into a new phase (denoted α) forming two atomic stripes with an angle of 60° (Figure 4a). Each strip of atoms consists of three to four constricted MoS₂ zig-zag chains with reduced Mo-Mo distance measured using STEM. At the intersection of the two stripes, the atoms are so packed that it triggers the formation of the 1T phase to release the strain. As the e-beam irradiation of the MoS₂ layer continues, the 1T phase domain progressively grows forming a triangular shape. The boundary of the 1T triangle with the 2 phases shows two new atomic arrangements denoted β and γ (Figure 4a). Thus electron beam can be used to very precisely pattern TMDs with alternating 1T and 2H phases, allowing for the creation of well defined geometries with abrupt metal-semiconductor

interfaces. Alternatively, phase transitions have also been observed from the electron transfer of plasmonic hot electrons to CVD grown MoS₂⁸⁸. Gold nanoparticles were used as plasmonic nanoparticles and deposited on the surface of TMDs (typically MoS₂) with a loading density of 10⁴ μm⁻². Under light exposure, the hot electrons are transferred to MoS₂ crystals. The 1T phase formation was confirmed by PL measurements and Raman spectroscopy.

Tensile or compressive strain can be also be used to tune the properties of TMDs. Several contributions have demonstrated that it is possible to modify the photoluminescence signals of group-6 TMDs via strain engineering. A recent report from Duerloo and coworkers has introduced the possibility of thermodynamically inducing phase transition through mechanical deformation of the group-6 TMDs⁸⁹. According to their calculations, the conversion from the 1H phase to the distorted WTe₂-like 1T phase can be achieved by applying strain on the TMD structure. The percent strain required to achieve the phase transition depends on the specific TMD used, but is still below the threshold for breaking the TMD layers. Best candidate for such mechanical switching of the structural phase is MoTe₂ with a minimal tensile strain of 0.3-3% at room temperature. These predictions allow imagining that phase transition could be achieved by depositing the crystals on bended flexible substrate or by using atomic force microscopy (Figure 4b).

Several groups have reported the chemical synthesis of TMDs via colloidal synthesis⁹⁰⁻⁹² or hydrothermal reaction⁹³. This method enables the synthesis of large quantity of few-layered thin TMDs via various types of precursors. Hybrid materials such as TMD/reduced graphene oxide (rGO) can be synthesized this way^{94,95}. By changing the synthesis conditions different concentrations of defects (vacancies, oxygen atoms) can be incorporated in the TMD atomic structure, which has been found to improve the catalytic activity towards the hydrogen evolution reaction^{96,97}. Colloidal synthesis could also be used for the synthesis of alloy-based

TMDs with various transition metals or chalcogens. The most thermodynamically stable phase is typically obtained via colloidal synthesis, which limits the possibility of tuning the crystal phases. Recent work from Ozin's group has demonstrated the possibility of controlling the synthesis of enriched 1T phase of WS_2 ⁹⁸. The modification of the reaction conditions in order to slow the reaction rate induces the preferential growth of single-layer 1T phase. The 1T nanosheets are negatively charged, which prevents aggregation. The nanosheets present a distorted structure similar to the structure of chemically exfoliated 1T WS_2 prepared via lithium intercalation¹⁸. Further improvements of the colloidal synthesis of TMD nanosheets is expected to open new directions towards the growth highly crystalline 1T and 1H phases.

The recent progress in chemical vapor deposition (CVD) or the epitaxial growth open new avenues for realizing phase engineering in TMDs while maintaining high degree of crystallinity. The most common way to grow TMDs by CVD is to use metal oxide and the chalcogen powders as source of transition metal and chalcogen, respectively^{49,50}.

Alternatively, few examples of liquid precursor such as thiomolybdate can be found in the literature⁹⁹. As discussed earlier in this review, few examples of alloys of CVD-grown TMD have been reported. Single-layers of mixed TMDs with lateral or vertical heterojunctions have been prepared via epitaxial growth⁴³⁻⁴⁵. Chemical vapor deposition favors growth of the most stable phase and thus the possibility of obtaining different phases is limited. Chemical vapor deposition based growth of TMDs with different phases that are usually not stable such as the 1T phase for the group 6 would open new possibilities to the field. Such growth has not been reported to date. However, Wypych et al. reported the growth of pure and highly crystalline bulk 1T MoS_2 by the sulfurization of potassium molybdate¹⁰⁰. Potassium molybdate K_2MoO_4 was first sulfurized at $T < 500^\circ\text{C}$ for 24 hours followed by reduction at 850°C for 72 hours under a flow of H_2/N_2 . This yields bulk KMoS_2 crystals with highly crystalline 1T phase of MoS_2 as confirmed using XRD diffraction. The presence of potassium counter ion in the

materials stabilizes the 1T phase and favors its formation. The crystal can then be washed with water to remove the potassium cations.

J. Stability of the 1T Phase

Engineering the phases of TMDs has been considered illusive due to the fact that TMDs have usually one phase that is thermodynamically stable. Yet the most stable 2H (1T) phase can be converted to the 1T (2H) phase. Up to now, most of the efforts have been focused on group 6 TMDs. Various characterization techniques including STEM, TEM, electron diffraction, Raman and XPS spectroscopy have confirmed the stability of the 1T phase at ambient conditions in absence of lithium^{13,24} in agreement with theoretical predictions^{26,75}. The origin of the stability of the 1T phase is probably due to structural distortion and the presence of counter ions. The presence of dopant impurities such as Au or Re may also contribute to the stabilization⁶². Heising and Kanatzidis demonstrated that exfoliated 1T nanosheets are negatively charged with a charge excess of ~ 0.3 charges per MX_2 ¹¹. The quantity of charges is however reduced compared to the initial stoichiometry of intercalated materials: $\text{Li}_{-1}\text{MX}_2$. Some of the charges react with water forming hydrogen H_2 during the exfoliation process. The reduction of the charges could explain why the metal atoms form zig-zag patterns in the case of exfoliated 1T MoS_2/WS_2 and calculations have predicted that with excess charges corresponding to $d^{2.0-2.5}$, zig-zag chains of Mo atoms are more favored¹⁰¹. The charges carried by 1T MoS_2/WS_2 can be reduced by using mild oxidizing agent such Br_2 or I_2 as confirmed by Zeta potential measurements⁸¹. Even after the quenching of the charges, the distorted ($2a \times a$) 1T phase is present according to Raman spectroscopy and STEM⁸¹. Heising and Kanatzidis have also observed distorted 1T phase with ($2a \times a$) and ($\sqrt{3}a \times \sqrt{3}a$) lattice with WS_2 and MoS_2 , respectively, treated with Br_2 ¹¹. DSC measurements of 1T MoS_2 and WS_2 have shown that the 1T to 1H transition occurs at significantly higher temperatures in the case of 1T WS_2 ($\sim 195^\circ\text{C}$) compared to 1T MoS_2 ($\sim 95^\circ\text{C}$). Interestingly the oxidation of 1T WS_2

and 1T MoS₂ with Br₂ induces a decrease in the transition temperature at ~ 145°C and ~ 90°C respectively, suggesting the role of the charges (and counter-ions) on the stability of the phase engineered TMDs^{11,80}. This relatively high transition temperature indicates that although the 2H phase is more stable, there is an energy barrier as high as ~ 0.87 eV for the 1T to 2H transformation²⁴ in good agreement with DFT calculations: 0.95 eV⁸⁰.

III. Conclusions and Perspectives

We have highlighted key progress in phase engineering of single layered transition metal dichalcogenides. Phase engineering in TMDs offers opportunities for doing both fundamental and technologically relevant research. Researchers are therefore actively involved in elucidating new methods for phase engineering in TMDs. Currently, phase engineering has been achieved by alkali metal intercalation, electron beam irradiation and strain engineering. Of these, lithium intercalation has a long history and thus has been widely studied. Recent results on fabrication of lateral heterostructures of metallic and semiconducting phases have led to the realization of novel electronic devices with very low contact resistances. Phase engineering has also benefitted in making better catalysts. Thus there is a tremendous amount of interest in this topic.

Although TMDs can exist in a variety of different phases, the main trick is to engineer those phases in a desired manner in the same material. That is to induce the metallic 1T phase in a semiconducting 1H TMD and vice versa. Presently it is not possible to realize single layer 1T phase TMD compounds due to stability issues. This has hampered progress in fundamental research because the 1T phase in two-dimensional systems could hold novel condensed matter phenomena. Our approach is to induce the 1T phase in stable 1H phase materials. The ability of fully converting a 1H phase TMD into 1T phase TMD will allow investigations of novel properties of the metallic phase.

References:

1. J. A. Wilson and A. D. Yoffe, *Adv. Phys.*, 1969, **18**, 193–335.
2. K. S. Novoselov, D. Jiang, F. Schedin, T. J. Booth, V. V. Khotkevich, S. V. Morozov, and A. K. Geim, *Proc. Natl. Acad. Sci. U. S. A.*, 2005, **102**, 10451–10453.
3. L. F. Mattheiss, *Phys. Rev. B*, 1973, **8**, 3719–3740.
4. Q. H. Wang, K. Kalantar-Zadeh, A. Kis, J. N. Coleman, and M. S. Strano, *Nanotechnol.*, 2012, **7**, 699–712.
5. P. Joensen, R. F. Frindt, and S. R. Morrison, *Mater. Res. Bull.*, 1986, **21**, 457–461.
6. B. K. Miremadi and S. R. Morrison, *J. Appl. Phys.*, 1988, **63**, 4970–4974.
7. S. Jiménez Sandoval, D. Yang, R. F. Frindt, and J. C. Irwin, *Phys. Rev. B*, 1991, **44**, 3955–3962.
8. D. Yang, S. J. Sandoval, W. M. Divigalpitiya, J. C. Irwin, and R. F. Frindt, *Phys. Rev. B Condens. Matter*, 1991, **43**, 12053–12056.
9. R. A. Gordon, D. Yang, E. D. Crozier, D. T. Jiang, and R. F. Frindt, *Phys. Rev. B*, 2002, **65**, 125407.
10. M. A. Py and R. R. Haering, *Can. J. Phys.*, 1983, **61**, 76–84.
11. J. Heising and M. G. Kanatzidis, *J. Am. Chem. Soc.*, 1999, **121**, 11720–11732.
12. P. Ganal, W. Olberding, T. Butz, and G. Ouvrard, *Solid State Ion.*, 1993, **59**, 313–319.
13. G. Eda, T. Fujita, H. Yamaguchi, D. Voiry, M. Chen, and M. Chhowalla, *ACS Nano*, 2012, **6**, 7311–7317.
14. F. Wypych, T. Weber, and R. Prins, *Chem. Mater.*, 1998, **10**, 723–727.
15. X. R. Qin, D. Yang, R. F. Frindt, and J. C. Irwin, *Phys. Rev. B*, 1991, **44**, 3490–3493.
16. X. R. Qin, D. Yang, R. F. Frindt, and J. C. Irwin, *Ultramicroscopy*, 1992, **42–44**, Part 1, 630–636.
17. J. Heising and M. G. Kanatzidis, *J. Am. Chem. Soc.*, 1999, **121**, 638–643.
18. D. Voiry, H. Yamaguchi, J. Li, R. Silva, D. C. B. Alves, T. Fujita, M. Chen, T. Asefa, V. B. Shenoy, G. Eda, and M. Chhowalla, *Nat. Mater.*, 2013, **12**, 850–855.
19. R. Kappera, D. Voiry, S. E. Yalcin, B. Branch, G. Gupta, A. D. Mohite, and M. Chhowalla, *Nat. Mater.*, 2014, **13**, 1128–1134.

20. S. Tongay, H. Sahin, C. Ko, A. Luce, W. Fan, K. Liu, J. Zhou, Y.-S. Huang, C.-H. Ho, J. Yan, D. F. Ogletree, S. Aloni, J. Ji, S. Li, J. Li, F. M. Peeters, and J. Wu, *Nat. Commun.*, 2014, **5**, 3252.
21. T. Fujita, Y. Ito, Y. Tan, H. Yamaguchi, D. Hoko, A. Hirata, D. A. Voiry, M. Chhowalla, and M. Chen, *Nanoscale*, 2014.
22. M. Kertesz and R. Hoffmann, *J. Am. Chem. Soc.*, 1984, **106**, 3453–3460.
23. D. Yang and R. F. Frindt, *J. Phys. Chem. Solids*, 1996, **57**, 1113–1116.
24. D. Voiry, H. Yamaguchi, J. Li, R. Silva, D. C. B. Alves, T. Fujita, M. Chen, T. Asefa, V. B. Shenoy, G. Eda, and M. Chhowalla, *Nat. Mater.*, 2013, **12**, 850–855.
25. M. Calandra, *Phys. Rev. B*, 2013, **88**, 245428.
26. M. Kan, J. Y. Wang, X. W. Li, S. H. Zhang, Y. W. Li, Y. Kawazoe, Q. Sun, and P. Jena, *J. Phys. Chem. C*, 2014, **118**, 1515–1522.
27. P. Johari and V. B. Shenoy, *ACS Nano*, 2012, **6**, 5449–5456.
28. M. Ghorbani-Asl, S. Borini, A. Kuc, and T. Heine, *Phys. Rev. B*, 2013, **87**, 235434.
29. L. Kou, A. Du, C. Chen, and T. Frauenheim, *Nanoscale*, 2014, **6**, 5156–5161.
30. P. Lu, X. Wu, W. Guo, and X. C. Zeng, *Phys. Chem. Chem. Phys.*, 2012, **14**, 13035–13040.
31. H. Peelaers and C. G. Van de Walle, *Phys. Rev. B*, 2012, **86**, 241401.
32. L. Yang, X. Cui, J. Zhang, K. Wang, M. Shen, S. Zeng, S. A. Dayeh, L. Feng, and B. Xiang, *Sci. Rep.*, 2014, **4**.
33. J. H. Lee, W. S. Jang, S. W. Han, and H. K. Baik, *Langmuir*, 2014, **30**, 9866–9873.
34. N. Lu, H. Guo, L. Li, J. Dai, L. Wang, W.-N. Mei, X. Wu, and X. C. Zeng, *Nanoscale*, 2014, **6**, 2879–2886.
35. H. J. Conley, B. Wang, J. I. Ziegler, R. F. Haglund, S. T. Pantelides, and K. I. Bolotin, *Nano Lett.*, 2013, **13**, 3626–3630.
36. K. He, C. Poole, K. F. Mak, and J. Shan, *Nano Lett.*, 2013, **13**, 2931–2936.
37. C. R. Zhu, G. Wang, B. L. Liu, X. Marie, X. F. Qiao, X. Zhang, X. X. Wu, H. Fan, P. H. Tan, T. Amand, and B. Urbaszek, *Phys. Rev. B*, 2013, **88**, 121301.
38. A. Castellanos-Gomez, R. Roldán, E. Cappelluti, M. Buscema, F. Guinea, H. S. J. van der Zant, and G. A. Steele, *Nano Lett.*, 2013, **13**, 5361–5366.
39. Y. Y. Hui, X. Liu, W. Jie, N. Y. Chan, J. Hao, Y.-T. Hsu, L.-J. Li, W. Guo, and S. P. Lau, *ACS Nano*, 2013, **7**, 7126–7131.
40. L. Kou, T. Frauenheim, and C. Chen, *J. Phys. Chem. Lett.*, 2013, **4**, 1730–1736.
41. H.-P. Komsa and A. V. Krasheninnikov, *Phys. Rev. B*, 2013, **88**, 085318.

42. G. Gao, W. Gao, E. Cannuccia, J. Taha-Tijerina, L. Balicas, A. Mathkar, T. N. Narayanan, Z. Liu, B. K. Gupta, J. Peng, Y. Yin, A. Rubio, and P. M. Ajayan, *Nano Lett.*, 2012, **12**, 3518–3525.
43. Y. Gong, J. Lin, X. Wang, G. Shi, S. Lei, Z. Lin, X. Zou, G. Ye, R. Vajtai, B. I. Yakobson, H. Terrones, M. Terrones, B. K. Tay, J. Lou, S. T. Pantelides, Z. Liu, W. Zhou, and P. M. Ajayan, *Nat. Mater.*, 2014, **13**, 1135–1142.
44. C. Huang, S. Wu, A. M. Sanchez, J. J. P. Peters, R. Beanland, J. S. Ross, P. Rivera, W. Yao, D. H. Cobden, and X. Xu, *Nat. Mater.*, 2014.
45. X. Duan, C. Wang, J. C. Shaw, R. Cheng, Y. Chen, H. Li, X. Wu, Y. Tang, Q. Zhang, A. Pan, J. Jiang, R. Yu, Y. Huang, and X. Duan, *Nat. Nanotechnol.*, 2014, **9**, 1024–1030.
46. T. Jiang, H. Liu, D. Huang, S. Zhang, Y. Li, X. Gong, Y.-R. Shen, W.-T. Liu, and S. Wu, *Nat. Nanotechnol.*, 2014, **9**, 825–829.
47. A. M. van der Zande, J. Kunstmann, A. Chernikov, D. A. Chenet, Y. You, X. Zhang, P. Y. Huang, T. C. Berkelbach, L. Wang, F. Zhang, M. S. Hybertsen, D. A. Muller, D. R. Reichman, T. F. Heinz, and J. C. Hone, *Nano Lett.*, 2014, **14**, 3869–3875.
48. S. Huang, X. Ling, L. Liang, J. Kong, H. Terrones, V. Meunier, and M. S. Dresselhaus, *Nano Lett.*, 2014, **14**, 5500–5508.
49. S. Najmaei, Z. Liu, W. Zhou, X. Zou, G. Shi, S. Lei, B. I. Yakobson, J.-C. Idrobo, P. M. Ajayan, and J. Lou, *Nat. Mater.*, 2013, **12**, 754–759.
50. A. M. van der Zande, P. Y. Huang, D. A. Chenet, T. C. Berkelbach, Y. You, G.-H. Lee, T. F. Heinz, D. R. Reichman, D. A. Muller, and J. C. Hone, *Nat. Mater.*, 2013, **12**, 554–561.
51. X. Yin, Z. Ye, D. A. Chenet, Y. Ye, K. O'Brien, J. C. Hone, and X. Zhang, *Science*, 2014, **344**, 488–490.
52. Y. Zhang, Y. Zhang, Q. Ji, J. Ju, H. Yuan, J. Shi, T. Gao, D. Ma, M. Liu, Y. Chen, X. Song, H. Y. Hwang, Y. Cui, and Z. Liu, *ACS Nano*, 2013, **7**, 8963–8971.
53. W. Zhou, X. Zou, S. Najmaei, Z. Liu, Y. Shi, J. Kong, J. Lou, P. M. Ajayan, B. I. Yakobson, and J.-C. Idrobo, *Nano Lett.*, 2013, **13**, 2615–2622.
54. Z. Zhang, X. Zou, V. H. Crespi, and B. I. Yakobson, *ACS Nano*, 2013, **7**, 10475–10481.
55. H. Li, X. Duan, X. Wu, X. Zhuang, H. Zhou, Q. Zhang, X. Zhu, W. Hu, P. Ren, P. Guo, L. Ma, X. Fan, X. Wang, J. Xu, A. Pan, and X. Duan, *J. Am. Chem. Soc.*, 2014, **136**, 3756–3759.
56. Y. Gong, Z. Liu, A. R. Lupini, G. Shi, J. Lin, S. Najmaei, Z. Lin, A. L. Elías, A. Berkdemir, G. You, H. Terrones, M. Terrones, R. Vajtai, S. T. Pantelides, S. J. Pennycook, J. Lou, W. Zhou, and P. M. Ajayan, *Nano Lett.*, 2014, **14**, 442–449.
57. J. Mann, Q. Ma, P. M. Odenthal, M. Isarraraz, D. Le, E. Preciado, D. Barroso, K. Yamaguchi, G. von Son Palacio, A. Nguyen, T. Tran, M. Wurch, A. Nguyen, V. Klee, S. Bobek, D. Sun, T. F. Heinz, T. S. Rahman, R. Kawakami, and L. Bartels, *Adv. Mater.*, 2014, **26**, 1399–1404.

58. S.-H. Su, Y.-T. Hsu, Y.-H. Chang, M.-H. Chiu, C.-L. Hsu, W.-T. Hsu, W.-H. Chang, J.-H. He, and L.-J. Li, *Small*, 2014, **10**, 2589–2594.
59. A. Kutana, E. S. Penev, and B. I. Yakobson, *Nanoscale*, 2014, **6**, 5820.
60. J. Xi, T. Zhao, D. Wang, and Z. Shuai, *J. Phys. Chem. Lett.*, 2014, **5**, 285–291.
61. Y.-C. Lin, D. O. Dumcenco, H.-P. Komsa, Y. Niimi, A. V. Krasheninnikov, Y.-S. Huang, and K. Suenaga, *Adv. Mater.*, 2014, **26**, 2857–2861.
62. Y.-C. Lin, D. O. Dumcenco, Y.-S. Huang, and K. Suenaga, *Nat. Nanotechnol.*, 2014, **9**, 391–396.
63. Y. Chen, J. Xi, D. O. Dumcenco, Z. Liu, K. Suenaga, D. Wang, Z. Shuai, Y.-S. Huang, and L. Xie, *ACS Nano*, 2013, **7**, 4610–4616.
64. Q. Feng, Y. Zhu, J. Hong, M. Zhang, W. Duan, N. Mao, J. Wu, H. Xu, F. Dong, F. Lin, C. Jin, C. Wang, J. Zhang, and L. Xie, *Adv. Mater.*, 2014, **26**, 2648–2653.
65. S. Tongay, D. S. Narang, J. Kang, W. Fan, C. Ko, A. V. Luce, K. X. Wang, J. Suh, K. D. Patel, V. M. Pathak, J. Li, and J. Wu, *Appl. Phys. Lett.*, 2014, **104**, 012101.
66. D. O. Dumcenco, H. Kobayashi, Z. Liu, Y.-S. Huang, and K. Suenaga, *Nat. Commun.*, 2013, **4**, 1351.
67. S. McDonnell, R. Addou, C. Buie, R. M. Wallace, and C. L. Hinkle, *ACS Nano*, 2014, **8**, 2880–2888.
68. S. Tongay, J. Suh, C. Ataca, W. Fan, A. Luce, J. S. Kang, J. Liu, C. Ko, R. Raghunathanan, J. Zhou, F. Ogletree, J. Li, J. C. Grossman, and J. Wu, *Sci. Rep.*, 2013, **3**.
69. M. Makarova, Y. Okawa, and M. Aono, *J. Phys. Chem. C*, 2012, **116**, 22411–22416.
70. S. S. Chou, M. De, J. Kim, S. Byun, C. Dykstra, J. Yu, J. Huang, and V. P. Dravid, *J. Am. Chem. Soc.*, 2013, **135**, 4584–4587.
71. L. P. Hansen, Q. M. Ramasse, C. Kisielowski, M. Brorson, E. Johnson, H. Topsøe, and S. Helveg, *Angew. Chem. Int. Ed.*, 2011, **50**, 10153–10156.
72. I. Samaras, S. I. Saikh, C. Julien, and M. Balkanski, *Mater. Sci. Eng. B*, 1989, **3**, 209–214.
73. M. B. Dines, *Mater. Res. Bull.*, 1975, **10**, 287–291.
74. M. S. Whittingham and F. R. Gamble Jr., *Mater. Res. Bull.*, 1975, **10**, 363–371.
75. A. N. Enyashin and G. Seifert, *Comput. Theor. Chem.*, 2012, **999**, 13–20.
76. M. Kan, J. Y. Wang, X. W. Li, S. H. Zhang, Y. W. Li, Y. Kawazoe, Q. Sun, and P. Jena, *J. Phys. Chem. C*, 2014, **118**, 1515–1522.
77. L. Wang, Z. Xu, W. Wang, and X. Bai, *J. Am. Chem. Soc.*, 2014, **136**, 6693–6697.
78. P. Joensen, R. F. Frindt, and S. R. Morrison, *Mater. Res. Bull.*, 1986, **21**, 457–461.

79. G. Eda, H. Yamaguchi, D. Voiry, T. Fujita, M. Chen, and M. Chhowalla, *Nano Lett.*, 2011, **11**, 5111–5116.
80. H.-L. Tsai, J. Heising, J. L. Schindler, C. R. Kannewurf, and M. G. Kanatzidis, *Chem. Mater.*, 1997, **9**, 879–882.
81. D. Voiry, M. Salehi, R. Silva, T. Fujita, M. Chen, T. Asefa, V. B. Shenoy, G. Eda, and M. Chhowalla, *Nano Lett.*, 2013, **13**, 6222–6227.
82. Z. Zeng, Z. Yin, X. Huang, H. Li, Q. He, G. Lu, F. Boey, and H. Zhang, *Angew. Chem. Int. Ed.*, 2011, **50**, 11093–11097.
83. Z. Zeng, T. Sun, J. Zhu, X. Huang, Z. Yin, G. Lu, Z. Fan, Q. Yan, H. H. Hng, and H. Zhang, *Angew. Chem. Int. Ed.*, 2012, **51**, 9052–9056.
84. A. Lerf and R. Schoellhorn, *Inorg. Chem.*, 1977, **16**, 2950–2956.
85. C. Lee, H. Yan, L. E. Brus, T. F. Heinz, J. Hone, and S. Ryu, *ACS Nano*, 2010, **4**, 2695–2700.
86. C. A. Papageorgopoulos and W. Jaegermann, *Surf. Sci.*, 1995, **338**, 83–93.
87. J. Zheng, H. Zhang, S. Dong, Y. Liu, C. Tai Nai, H. Suk Shin, H. Young Jeong, B. Liu, and K. Ping Loh, *Nat. Commun.*, 2014, **5**.
88. Y. Kang, S. Najmaei, Z. Liu, Y. Bao, Y. Wang, X. Zhu, N. J. Halas, P. Nordlander, P. M. Ajayan, J. Lou, and Z. Fang, *Adv. Mater.*, 2014, **26**, 6467–6471.
89. K.-A. N. Duerloo, Y. Li, and E. J. Reed, *Nat. Commun.*, 2014, **5**.
90. X. Zhou, J. Jiang, T. Ding, J. Zhang, B. Pan, J. Zuo, and Q. Yang, *Nanoscale*, 2014, **6**, 11046–11051.
91. D. Yoo, M. Kim, S. Jeong, J. Han, and J. Cheon, *J. Am. Chem. Soc.*, 2014, **136**, 14670–14673.
92. P. Miró, J. H. Han, J. Cheon, and T. Heine, *Angew. Chem. Int. Ed.*, 2014, **46**, 12624–12628.
93. Chen and R. Fan, *Chem. Mater.*, 2001, **13**, 802–805.
94. Y. Li, H. Wang, L. Xie, Y. Liang, G. Hong, and H. Dai, *J. Am. Chem. Soc.*, 2011, **133**, 7296–7299.
95. J. Yang, D. Voiry, A. Y. Kim, M. Chhowalla, and H. S. Shin, *Angew. Chem. Int. Ed.*, 2013, **52**, 13751–13754.
96. J. Xie, H. Zhang, S. Li, R. Wang, X. Sun, M. Zhou, J. Zhou, X. W. (David) Lou, and Y. Xie, *Adv. Mater.*, 2013, **25**, 5807–5813.
97. J. Xie, J. Zhang, S. Li, F. Grote, X. Zhang, H. Zhang, R. Wang, Y. Lei, B. Pan, and Y. Xie, *J. Am. Chem. Soc.*, 2013, **135**, 17881–17888.
98. B. Mahler, V. Hoepfner, K. Liao, and G. A. Ozin, *J. Am. Chem. Soc.*, 2014, **136**, 14121–14127.

99. K.-K. Liu, W. Zhang, Y.-H. Lee, Y.-C. Lin, M.-T. Chang, C.-Y. Su, C.-S. Chang, H. Li, Y. Shi, H. Zhang, C.-S. Lai, and L.-J. Li, *Nano Lett.*, 2012, **12**, 1538–1544.
100. F. Wypych and R. Schöllhorn, *J. Chem. Soc. Chem. Commun.*, 1992, 1386–1388.
101. J. K. Burdett and T. Hughbanks, *Inorg. Chem.*, 1985, **24**, 1741–1750.

Figures:

Fig. 1: Different polymorphs or phases of single-layer and stacked single-layer TMDs: (A) 1T phase, (B) ideal ($a \times a$) 1T phase, (C) distorted ($2a \times a$) 1T phase, (D) 2H phase and (E) 3R phase. (F) Scanning Transmission Electron Microscope (STEM) images of single-layer MoS_2 showing a boundary between the 1T and 2H phases. The Arrow indicates the boundary between the phases. Scale bar: 5nm. Reproduced with permission from ref. 19. Copyright 2014, Nature Publishing Group. (G) STEM image of a lithiated single-layer ReS_2 . After lithiation, the Re atoms form rhombus clusters. Reproduced from ref. 21 with permission from The Royal Society of Chemistry. (H) STEM image of a grain boundary in CVD-grown single-layer MoS_2 . The grain boundary is formed of five- and seven-fold rings (5|7) and dislocations with six- and eight-fold rings (6|8). Reproduced with permission from ref. 53. Copyright 2013, American Chemical Society.

Fig. 2: (A) Optical image of triangular MoSe_2 – WSe_2 heterostructure crystals grown by physical vapor transport. The core of the triangles consists in MoSe_2 whereas WSe_2 epitaxially grows on the MoSe_2 edges. (B) Top: Color map of the chemical composition of the MoSe_2 – WSe_2 heterostructure observed by STEM. The chemical composition is obtained by the scattered electron intensity. Bottom: Restructured structures of the same region. Scale bar: 1nm. Reproduced with permission from ref. 44. Copyright 2014, Nature Publishing Group. (C) Modification of the photoluminescence spectra of single-layer MoS_2 upon the application

of tensile strain. Inset: Band structure for single-layer MoS₂ for 0% (black), ~5% (maroon) and ~8% (red) of strain. Reproduced with permission from ref. 35. Copyright 2013, American Chemical Society. (D) Optical images of twisted bilayer MoS₂ with an angle of 34°. (E) Photoluminescence (PL) spectra of bilayer of MoS₂ with twisting angle from 0° (black) to 60° (yellow). PL spectra from the top and bottom layer are shown in grey and light blue respectively. Reproduced with permission from ref. 47. Copyright 2014, American Chemical Society. (F) Tuning of the PL response from MoS₂(1-x)Se_{2x}. Optical response for x = 0, x = 0.3, x = 0.5, x = 0.75 and x = 1 are shown in blue, green, purple, orange, and red respectively. Inset shows the comparison between the experimental (red) and the calculated (green) values of the band gap. Reproduced with permission from ref. 56. Copyright 2014, American Chemical Society.

Fig. 3: (A) Potential range of the different redox couples involved in the intercalation and the oxidation of the TMDs. The reduction (MX₂/MX₂ⁿ⁻) and oxidation (MX₂/MO_y) potential ranges of TMDs are indicated in blue and red respectively. (B) Evolution of the Raman spectra of chemically exfoliated MoS₂ at increasing annealing temperatures up to 300°C. As-exfoliated 1T MoS₂ exhibits additional signatures including the J₁, J₂ and J₃ signals. When increasing the annealing temperature, the signals from the 1T phase progressively decrease. (C) High-resolution X-ray photoelectron spectra from the Mo3d and S2p regions of chemically exfoliated MoS₂. Each spectrum can be decomposed with 2 components from the 1T and the 2H phases. The signals from the 1T are found to be downshifted of ~ 0.8-0.9 eV relative to the 2H signals. Reproduced with permission from ref. 79. Copyright 2011, American Chemical Society.

Fig. 4: (A) 2H to 1T transformation of a single-layer of MoS₂ under electron-beam irradiation. After 100s, a new phase (denoted α) forms on the MoS₂ basal plane forming two stripes with an angle of 60°. Rapidly the 2H phase between the two stripes convert to the 1T phase. As time increases, the 1T phase domains grow and two new types of boundary denoted

β and γ appear. Reproduced with permission from ref. 62. Copyright 2014, Nature Publishing Group. (B) 2H to 1T phase transformation of single-layer TMDs when applying uniaxial strain. The region quasi freely-suspended or on a low-friction substrate (middle) is converted. (C) Evolution of the free energy and the force when applying uniaxial deformation. In the beginning (step 1) the 2H phase deforms elastically without phase transition. In step 2, the lowest free-energy path is a common tangent between the 2H and distorted 1T (1T') energy surfaces and co-existence of both phases is predicted. This region corresponds to a plateau in the applied force. Increasing further the extension leads to the formation of 100% distorted 1T phase. Reproduced with permission from ref. 89. Copyright 2014, Nature Publishing Group.

